PNAS RESEARCH ARTICLE | CHEMISTRY

Synthetic control over proximity of metal and acid dual sites switches the selectivity of acetophenone hydrodeoxygenation

Luyan Li[a], Xinhui Guo[a], Jiajia Huang[a], Zhenhe Jia[b], Xiaoshuo Liu[c], Qiaoqiao Guan[a], Yu Gu[d], Weijie Yang[b], Junling Lu[a], Shaojun Guo[d,1], and Hai-Long Jiang[a,1]

Affiliations are included on p. 9.

Edited by Joanna Aizenberg, Harvard University, Allston, MA; received September 15, 2025; accepted March 22, 2026

Though spatial arrangement between metal and acid has proven efficiency for enhancing catalytic performance, their precise regulation on controlling the product selectivity and revealing related catalytic mechanism remains scarce. Herein, we report a class of Pd nanoparticles integrated into isoreticular UiO-66-type metal-organic frameworks with or without sulfonic acid groups (denoted UiO-S and UiO), which allows for precise distance tuning between Pd and acid site by controlling UiO-66 interlayer thickness. Unlike traditional studies focusing on substrate/intermediate diffusion by dual-site regulation, we herein demonstrate that significant modulation of electron transfer and proton concentration around Pd over UiO-S@UiO$_{25}$@Pd@UiO switches reaction pathways and profoundly tunes selectivity in acetophenone hydrodeoxygenation. Specifically, we show that UiO-S@UiO$_{25}$@Pd@UiO with a 25 nm separation between Pd and acid sites achieves the highest selectivity (~94%) to phenylethanol via homolytic H_2 cleavage, mitigating prevalent overhydrogenation pathway; whereas UiO-S@Pd@UiO and UiO@Pd@UiO-S, with closely positioned dual sites, dramatically enhance hydrodeoxygenation activity, and display >99% selectivity to high-energy-density ethylbenzene. Notably, a proton-assisted mechanism involving H_2 heterolysis is elucidated over UiO@Pd@UiO-S, particularly significant for implementing the catalytic process under mild conditions.

metal-organic framework | dual-site regulation | switchable selectivity | hydrodeoxygenation | homolytic/heterolytic cleavage

Significance

Bifunctional catalysts play vital roles and are widely used in catalysis. It is well established that the proximity of dual active sites determines catalytic performance. Yetspatial arrangement control over dual sites is restricted to two extremes, metal sites either embedded within or positioned on acidic porous supports. It remains a great challenge to systematically precisely regulate the distance between dual sites. Herein, by combining Pd nanoparticles and isoreticular multilayered UiO-66-type metal-organic frameworks with/without sulfonic acid groups, we successfully achieve precise nanoscale control of dual-site (Pd and acid sites) distance, allowing the switchable selectivity in acetophenone hydrodeoxygenation. The synthetic protocol and findings in this work will inspire further research and lay the foundation for developing other precisely regulated bifunctional catalysts.

Cooperation of two distinct active sites within a single catalyst is of great importance in many complex catalytic processes, such as selective hydrodeoxygenation of the C=O bond in biomass upgrading, hydroisomerization of light alkanes and others (1–3). Each active site in bifunctional catalysts works for individual step, and the substrates are sequentially exposed to different active sites prior to the generation of desired products (4–7). Up to date, plenty of bifunctional catalysts, such as oxide-zeolite composites, transition metal-solid acid composites, metal particles interfaced with organic acid-functionalized monolayers, etc., have been developed (1–17). Among them, metal nanoparticles (NPs), such as Pd and Pt, dispersed by solid acid supports such as zeolites, are mostly investigated (8–17). In these bifunctional catalysts, the proximity degree between the dual sites and their relative distribution influences the diffusion and adsorption of substates/intermediates, resulting in highly regulated catalytic performance (10–14). On account of this, continued efforts are devoted to controlling the distance and relative distribution of the dual sites. There have been two main hypotheses explaining their possible influences on catalytic performance. Traditional understanding is known as the intimacy criterion, simply interpreted as the closer proximity the better activity, for which encapsulating metal NPs inside the zeolites is thought to be favorable (14). However, recent investigations have revealed that a nanoscale rather than the closest intimacy between metal and acid sites is preferable in catalysis (10, 11). The metal NPs are deposited into and outside zeolites, respectively by ion exchange and electrostatic adsorption of metal precursors, leading to the closest proximity and nanoscale intimacy between metal and acid sites (10). Though the above understandings on bifunctional catalysts, the control on dual sites in functional catalysts is almost limited to be the two extremes, i.e., metal sites incorporated into and located on acid-involved porous matrices (10–12). The distance control between the dual sites is actually very difficult with the reported strategies, which are usually entangled with other perturbations (e.g., particle/pore sizes) (15–17). To gain in-depth insights into structural regulation on reaction mechanisms and performance, it is necessary to fabricate model catalytic systems precisely controlling spatial distribution of bifunctional sites, which, however, remains an unmet challenge.

In this context, crystalline porous materials would be highly desired supports when possessing the following features: i) high stability and surface area for loading tiny metal

Author contributions: H.-L.J. conceived the project and supervised the project; L.L. designed and performed the synthesis; X.G. and Q.G. assisted the synthesis; J.H., Z.J., X.L., and W.Y. conducted the theoretical calculations; Y.G., J.L., and S.G. analyzed data and discussed the results; S.G. and H.-L.J. revised the paper; and L.L. and H.-L.J. wrote the paper.

The authors declare no competing interest.

This article is a PNAS Direct Submission.

[1]To whom correspondence may be addressed. Email: guosj@pku.edu.cn or jianglab@ustc.edu.cn.

This article contains supporting information online at https://www.pnas.org/lookup/suppl/doi:10.1073/pnas.2526002123/-/DCSupplemental.

Published May 5, 2026.

NPs and ii) the atomically tailored and multivariate structures enabling the control of proximity and relative location of the dual sites. Metal-organic frameworks (MOFs) (18–24), a class of porous crystalline solids, not only involve acid sites on their skeletons but also show great promise to stabilize metal NPs (25–29). Particularly, MOFs with great structural flexibility, tolerability, and multivariate features would enable the distance control between the particular site on the skeleton and guest metal NPs, although this has never been achieved yet.

Based on the above considerations, a series of bifunctional composites, namely UiO-S@UiO_x@Pd@UiO (x = 0, 5.5, 14, 25, representing UiO-66 interlayer thickness) composites, have been elaborately fabricated using lattice-matched UiO-66 [simply as UiO, formulated $Zr_6O_4(OH)_4(BDC)_6$, BDC = benzenedicarboxylic acid] and UiO-66-SO_3H [simply as UiO-S, formulated $Zr_6O_4(OH)_4(BDC)_x(BDC\text{-}SO_3H)_{6-x}$, BDC-$SO_3H$ = 2-sulfoterephthalic acid]. The structure features a UiO-66-SO_3H core with Brønsted acid sites, encapsulated by UiO-66, Pd NPs, and an outer UiO-66 shell, where the thickness of UiO-66 spacing interlayer between Pd and UiO-66-SO_3H can be well modulated from 0 to 25 nm, achieving precise control of proximity degree between Pd-acid dual sites (Fig. 1). To further adjust functional site arrangement, an inverse structure, UiO@Pd@UiO-S, has also been constructed (Fig. 1, *Right*). These composites display distinctly different performance in the selective hydrodeoxygenation of acetophenone. The UiO-S@UiO_{25}@Pd@UiO presents ~94% selectivity to 1-phenylethanol via a traditional hydrogenation pathway due to minimal electron and proton effects between Pd and -SO_3H sites. Reducing the distance between the two sites increases conversion and shifts selectivity toward ethylbenzene are gradually improved. Significantly, both UiO-S@Pd@UiO without UiO-66 interlayer and UiO@Pd@UiO-S exhibit high selectivity to ethylbenzene due to enhanced proton concentration around Pd. Furthermore, due to strong Pd-acid interaction and proton-involved H_2 heterolysis pathway, UiO@Pd@UiO-S exhibits superior selectivity and activity to all UiO-S@UiO_x@Pd@UiO composites.

Results

The representative isoreticular Zr-MOFs, UiO-66, and UiO-66-SO_3H, with sizes of ~310 nm (*SI Appendix*, Fig. S1), were synthesized (30). In addition, Pd NPs with an average size of ~2.3 nm are also prepared (*SI Appendix*, Fig. S2) (31). To precisely regulate the dual site distance, UiO-66 was grown on UiO-66-SO_3H to give UiO-S@UiO_x core-shell structure with tunable UiO-66 shell thicknesses (0, 5.5, 14, 25 nm), due to their matched crystal lattice (Fig. 1 and *SI Appendix*, Figs. S3 *A* and *B* and S4). The Pd NPs were then assembled with UiO-S@UiO_x (x = 0, 5.5, 14, and 25) to obtain UiO-S@UiO_x@Pd composites, followed by overcoating with a ~25 nm UiO-66 shell to yield UiO-S@UiO_x@Pd@UiO, protect Pd from leaching (Fig. 2*A*). As a control, sandwich-structured UiO@Pd@UiO-S was fabricated by assembling Pd NPs onto UiO-66 particles, followed by epitaxial growth of UiO-66-SO_3H shell (Fig. 2*B* and *SI Appendix*, Fig. S3*C*) (32). Noteworthily, to guarantee consistent dual sites and uniform thickness of the outermost shell (for constant mass transfer), the UiO-66-SO_3H shell of ~25 nm is composed by BDC-SO_3H linker only in UiO@Pd@UiO-S, which is a bit different from the mixed BDC and BDC-SO_3H linkers for the UiO-66-SO_3H core in UiO-S@UiO_x@Pd@UiO. By choosing UiO-S@UiO_{25}@Pd@UiO and UiO@Pd@UiO-S as representative samples, elemental line-scans across slices reveal the distribution of Pd and S elements (Fig. 2 *C–E*). As expected, the distribution of S is restricted to the UiO-S core and separated from Pd NPs in UiO-S@UiO_{25}@Pd@UiO (Fig. 2*D*). A concurrent distribution of Pd and S can be observed in UiO@Pd@UiO-S, as also verified by the elemental mapping results (Fig. 2*E* and *SI Appendix*, Fig. S5). These results clearly confirm that the spatial distribution of Pd NPs and -SO_3H groups in different composites is precisely controlled as designed.

Powder X-ray diffraction patterns showcase the good crystallinity of all samples, with no visible Pd NP peaks due to their small size and low content (*SI Appendix*, Fig. S6*A*). N_2 sorption isotherms show comparable porosity and surface area for UiO-S@UiO_x@Pd@UiO (x = 0, 5.5, 14, and 25) and UiO@Pd@UiO-S (*SI Appendix*, Fig. S6*B*). All composites contain similar Pd amount (~1.0 wt%) by the inductively coupled plasma atomic emission spectrometry (ICP-AES) (*SI Appendix*, Table S1), and even comparable contents of -SO_3H group according to the S elemental analyses (*SI Appendix*, Table S1). Moreover, the ratio between Pd and Brønsted acid sites across samples is very similar based on the proton NMR (^{1}H NMR) and ICP-AES results (*SI Appendix*, Fig. S7 and Table S2).

X-ray photoelectron spectroscopy (XPS) reveals a shift in the Pd $3d_{5/2}$ peak toward higher binding energies along with reduced UiO_x interlayer thickness in UiO-S@UiO_x@Pd@UiO (x = 0, 5.5, 14, and 25) (Fig. 2*F* and *SI Appendix*, Table S3). The high binding energy of Pd $3d_{5/2}$ in UiO-S@Pd@UiO and UiO@Pd@UiO-S suggests electron transfer between closely positioned dual sites,

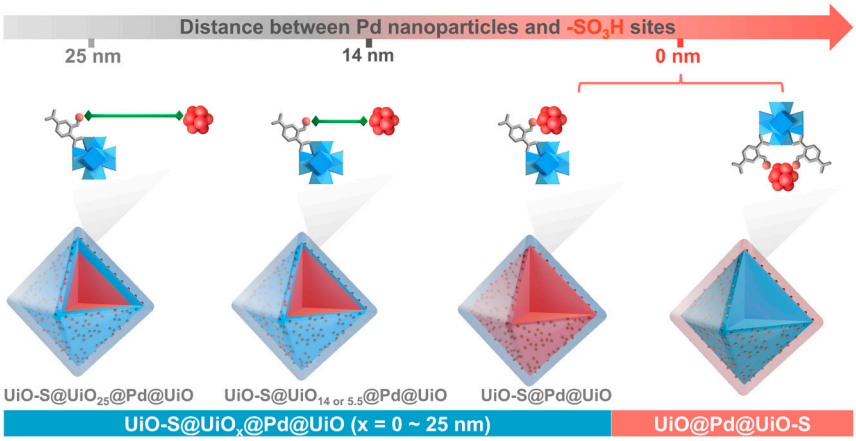

Fig. 1. Spatial arrangement regulation of the dual sites. Schematic illustration showing the precise regulation of spatial arrangement between Pd NPs (deep red) and the sulfonic acid group (orange) in UiO-S@UiO_x@Pd@UiO (x = 0, 5.5, 14, and 25) and UiO@Pd@UiO-S. The color of UiO_x spacing interlayer is deliberately diluted for easy recognition.

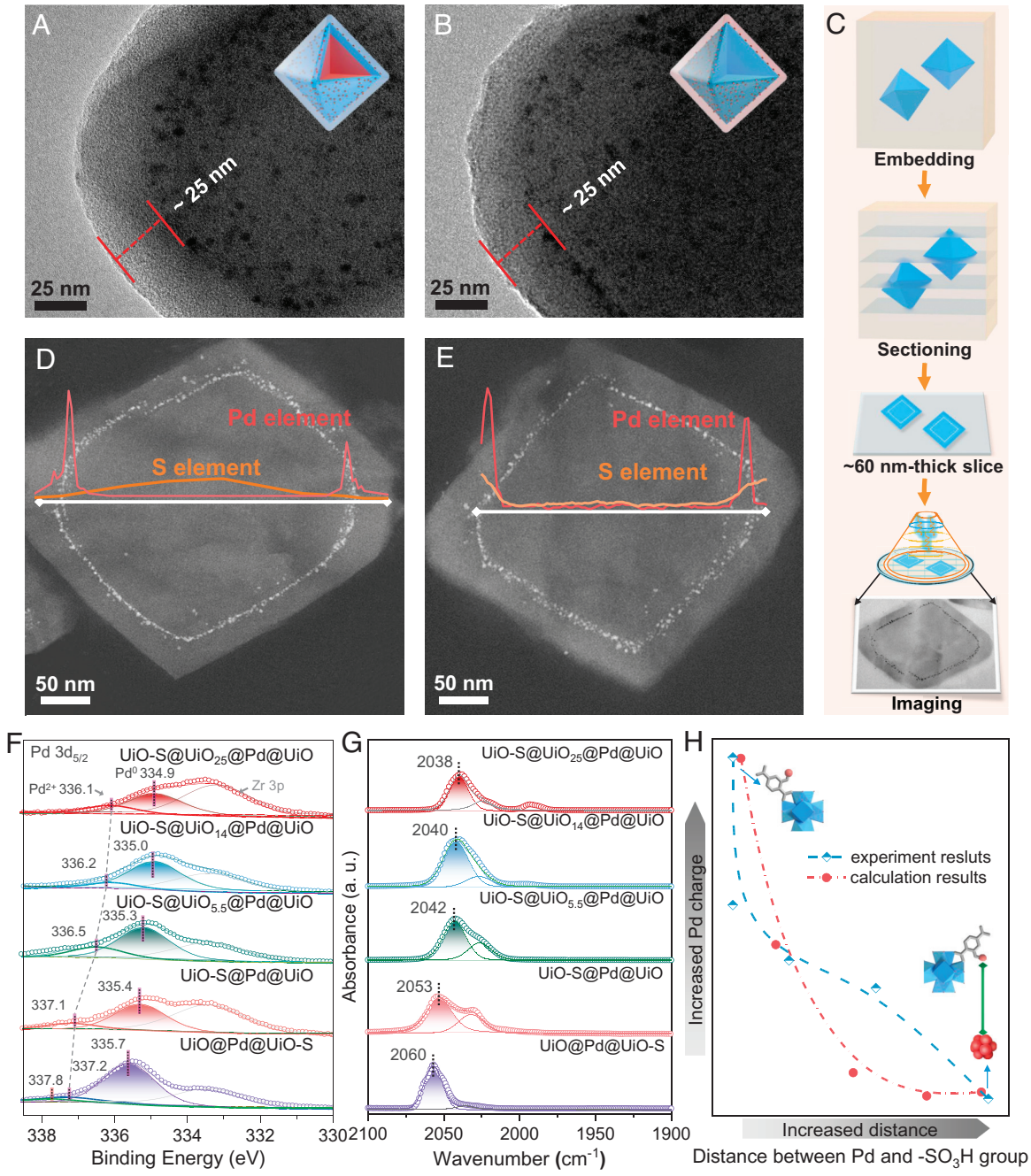

Fig. 2. Electron microscope and Pd electronic state characterizations. (*A* and *B*) Transmission electron microscopy (TEM) images of (*A*) UiO-S@UiO_{25}@Pd@UiO and (*B*) UiO@Pd@UiO-S (*Inset*: structural models). (*C*) Schematic diagram showing the sectioning of embedded catalyst particles to slices for electron microscopic characterizations. (*D* and *E*) High-angle annular dark-field scanning TEM (HAADF-STEM) images of UiO-S@UiO_{25}@Pd@UiO (*D*) and UiO@Pd@UiO-S slices. (*E*) (*Insets* in *D* and *E*: elemental line-scanning profiles of Pd and S elements), (*F*) XPS spectra and (*G*) CO-DRIFTS spectra for UiO-S@UiO_x@Pd@UiO (x = 0, 5.5, 14, and 25) and UiO@Pd@UiO-S composites. (*H*) Relationships between Pd charge and the dual-site distance.

driven by the electron-withdrawing effect of $-SO_3H$ groups around Pd NPs. Intriguingly, the binding energy of Pd $3d_{5/2}$ at 335.7 eV (Pd^0), 337.2 eV (Pd^{2+}), and 337.8 eV (Pd^{4+}) for UiO@Pd@UiO-S is slightly higher than that of UiO-S@Pd@UiO [335.4 eV (Pd^0) and 337.1 eV (Pd^{2+})] (Fig. 2*F*), due to the reduced concentration of $-SO_3H$ groups around Pd using mixed linkers in the latter. By contrast, in UiO-S@UiO_x@Pd@UiO (x = 5.5, 14, and 25) composites, such electron transfer is limited, owing to the spatial separation of the two sites. Diffuse reflectance infrared Fourier transform spectroscopy (DRIFTS) with CO as a probe shows a gradual blue shift in CO adsorption peaks (2,038 to 2,060 cm^{-1}) for UiO-S@UiO_x@Pd@UiO (x = 0, 5.5, 14, and 25) and UiO@Pd@UiO-S (Fig. 2*G*), indicative of reduced Pd electron density, which is in line with the above XPS results. In addition, this relationship between Pd valence and the dual site distance is also supported via the Pd charge calculation, which unveils that the close proximity between Pd and $-SO_3H$ sites causes enhanced electron interaction (Fig. 2*H* and *SI Appendix*, Fig. S8).

Encouraged by the results above, the selective hydrodeoxygenation of acetophenone over UiO-S@UiO_x@Pd@UiO (x = 0, 5.5, 14, and 25) and UiO@Pd@UiO-S composites for producing value-added 1-phenylethanol and/or ethylbenzene (33–35), has been investigated. To our delight, full conversion of acetophenone is observed within 3 h over all these composites,

including the controlled catalysts (x = 7.2, 84.5), at 60 °C with a H_2 balloon (Fig. 3*A* and *SI Appendix*, Table S4). In particular, UiO-S@UiO_{25}@Pd@UiO shows a high selectivity (~94%) to 1-phenylethanol in 3 h, and the selectivity even can be maintained at 90% after reacting for 36 h (*SI Appendix*, Table S4, entries 5 to 6). Instead, UiO-S@UiO_{25}@Pd@UiO shows the sluggish dehydration process by directly using 1-phenylethanol as the reactant with only 6% conversion (*SI Appendix*, Table S5). By reducing the UiO_x interlayer thickness, i.e., reduced distance between Pd and $-SO_3H$ sites, in UiO-S@UiO_x@Pd@UiO, steadily decreased 1-phenylethanol selectivity is observed (Fig. 3*A* and *SI Appendix*, Table S4). Notably, both UiO-S@Pd@UiO and UiO@Pd@UiO-S show high selectivity to ethylbenzene (>99%) after reacting for 3 h. Such outstanding ability for dehydration process is also verified by completely converting 1-phenylethanol to ethylbenzene (*SI Appendix*, Table S5). To fairly evaluate the selectivity difference, the conversion of acetophenone over different catalysts has been deliberately controlled at around 80% (*SI Appendix*, Fig. S9*A*). As a result, UiO@Pd@UiO-S exhibits high ethylbenzene selectivity, superior to that of all other counterparts. To assess the mass transfer resistance of UiO layer, the catalyst amount was adjusted from 0 mg to 15 mg for representative samples, UiO-S@UiO_{25}@Pd@UiO and UiO@Pd@UiO-S. The resultant linear correlation between catalyst amount and corresponding activity indicates negligible mass transfer resistance during reaction (*SI Appendix*, Fig. S9 *B* and *C*). Moreover, a control experiment with a thinner MOF layer (14 nm) and a proton concentration comparable to that of UiO-S@UiO_{25}@Pd@UiO yields 1-phenylethanol as the dominant product, confirming that the selectivity is independent of mass transfer limitations (*SI Appendix*, Table S6). The high apparent activation energy (E_a) values across different catalysts further corroborate that the reaction operates in a kinetically controlled regime (*SI Appendix*, Fig. S9 *D–F*).

These results preliminarily indicate that the selectivity of acetophenone transformation is directly related to the distance between Pd and acid sites. To further track the product formation over different composites, the reaction kinetics have been investigated and results reveal that acetophenone hydrodeoxygenation proceeds via two steps: I) carbonyl hydrogenation to 1-phenylethanol (C=O → C-O) and II) hydroxyl dehydration to ethylbenzene (36). The conversion of acetophenone is completed within 60 min over UiO-S@UiO_{25}@Pd@UiO. With reduced distance between Pd and acid sites, the conversion rate of acetophenone gradually increases, accompanying 1-phenylethanol converting to ethylbenzene. When the UiO_x interlayer is absent, the resulting UiO-S@Pd@UiO presents the highest conversion efficiency and complete ethylbenzene selectivity (>99%) among all UiO-S@UiO_x@Pd@UiO catalysts (Fig. 3 *B–E*). Interestingly, UiO@Pd@UiO-S exhibits even greater

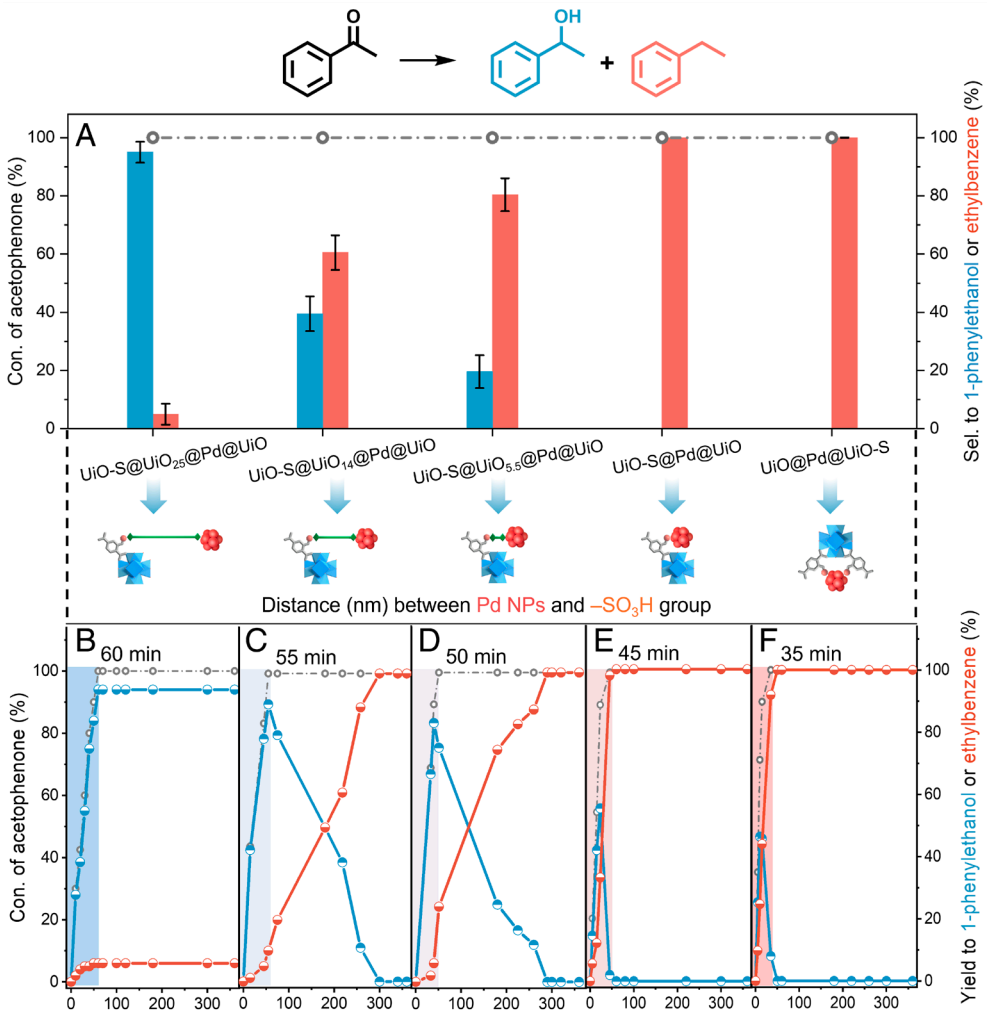

Fig. 3. Catalytic performance of acetophenone hydrodeoxygenation. (*A*) Catalytic results of acetophenone transformation over UiO-S@UiO_x@Pd@UiO (x = 0, 5.5, 14, and 25) and UiO@Pd@UiO-S in 3 h. Error bars represent the SD from three independent experiments. (*B–F*) Time-dependent conversion and selectivity of different catalysts in the hydrodeoxygenation of acetophenone. Reaction conditions: 15 mg of catalyst, 4 mL of EtOH, 24 μL of acetophenone, H_2 balloon, and 60 °C.

activity than UiO-S@Pd@UiO (Fig. 3*F*). The results unambiguously suggest that both proximity degree between the dual sites and concentration of –SO_3H group around Pd sites dominate the reaction process, leading to discriminative activity and selectivity.

Temperature-programmed desorption (TPD) is applied to evaluate decomposition of the metal-hydride phase on UiO-S@UiO_x@Pd@UiO (x = 5.5, 14, and 25 nm) and UiO@Pd@UiO-S. All H_2-TPD profiles display apparent decomposed peaks below 100 °C (*SI Appendix*, Fig. S10*A*), in accordance with the reported decomposition temperature of Pd-hydride species (37). Moreover, the decomposed temperature over different catalysts are in order of UiO@Pd@UiO-S > UiO-S@$UiO_{5.5}$@Pd@UiO > UiO-S@UiO_{14}@Pd@UiO > UiO-S@UiO_{25}@Pd@UiO, indicating a reduced bonding strength of Pd-H species. While similar trend for H_2 uptake ability is also observed (*SI Appendix*, Fig. S10*B*). The results reveal both strongest Pd-H interaction and highest concentration of active H species over UiO@Pd@UiO-S, which favors H_2 activation. Infrared spectra of acetophenone sorption have been also investigated to probe its adsorption on the catalysts. The bands 1,669 cm^{-1} on UiO-S@UiO_{25}@Pd@UiO and 1,694 cm^{-1} on UiO@Pd@UiO-S are ascribed to the C=O stretching vibration of acetophenone adsorbed on the Pd sites (*SI Appendix*, Fig. S11) (36). The shifted peak position likely arises from the differentiated valence of Pd NPs (38). During the thermal desorption process, the full desorption of acetophenone occurs at 110 °C on UiO-S@UiO_{25}@Pd@UiO, slightly lower than UiO@Pd@UiO-S (130 °C) (*SI Appendix*, Fig. S11). This indicates that acetophenone has stronger interaction with Pd sites in UiO@Pd@UiO-S, which would be favorable to the activation of acetophenone.

Deuterium-labeling experiments are conducted to understand the dissociation of H_2 molecules. When H_2 and D_2 are respectively employed as the reducing gas in the reaction, the rate constant ratio, KIE (K_L/K_H, where K_L and K_H are the rate constants for light and heavy substrates, respectively), in the acetophenone hydrodeoxygenation process over UiO@Pd@UiO-S reaches 5.81 (*SI Appendix*, Fig. S12*A*). This large isotope effect identifies the H_2 cleavage as the turnover-limiting step (39). Such a strong primary effect is generally reported in a proton-involved process (40), supporting the heterolysis of H_2 occurs to produce the H^+ species. The results reveal that the heterolytic cleavage of H_2 molecule serves as the turnover-limiting step in step I (C=O → C-O), which is probably due to the strong electron interaction between Pd NPs and the –SO_3H groups. Additionally, a KIE value of 5.91 is obtained by applying 1-phenylethanol as the substrate with other reaction conditions fixed (*SI Appendix*, Fig. S12*B*), indicating that the heterolytic dissociation of dihydrogen also occurs in the subsequent dehydration process (step II). In contrast to the high KIE values on UiO@Pd@UiO-S, much smaller KIE of the homolytic hydrogen splitting step with values of ~2.21 and ~2.77 is observed for UiO-S@UiO_{25}@Pd@UiO and UiO-S@Pd@UiO, respectively (*SI Appendix*, Fig. S12 *C* and *D*). The values reflect that the hydrogen homolysis step is involved in the turnover-limiting step (39), yet makes slightly different contributions in the reaction, where the larger value of 2.77 stands for the H_2 cleavage turnover-limiting step reflecting stronger influence on the reactivity over UiO-S@Pd@UiO catalyst. In addition to the KIE, the DRIFTS experiments with H_2 as probe molecules are also conducted (*SI Appendix*, Fig. S13). The result shows that the heterolysis of H_2 over UiO@Pd@UiO-S is accompanied with the appearance of O-$H^{\delta+}$ signal at ~ 3,500 cm^{-1}. This O-$H^{\delta+}$ species is formed probably due to the generated $H^{\delta+}$ species coordinating with O atoms of linkers in the UiO-S layer (41). Whereas the O-$H^{\delta+}$ signal is not detected over UiO-S@UiO_{25}@Pd@UiO where the homolytic hydrogen dissociation occurred.

Density functional theory (DFT) calculations support that the heterolytic cleavage of H_2 over Pd surface is preferential in the intimate model (simulating UiO@Pd@UiO-S), featuring a lower free energy barrier of 0.12 eV than the other counterparts, which is probably due to the strong electron transfer from –SO_3H groups to Pd surface (Fig. 4*A* and *SI Appendix*, Figs. S14–S16). In contrast, the homolytic cleavage of H_2 preferentially occurs in both intimate dual-site (with low-density acid sites simulating UiO-S@Pd@UiO) and separate dual-site (simulating UiO-S@UiO_{25}@Pd@UiO) models with a free energy barrier of 0.30 eV and 0.32 eV, respectively (Fig. 4 *B* and *C* and *SI Appendix*, Figs. S17–S20). Moreover, the free energy barrier of H_2 heterolysis on both intimate dual-site models (simulating UiO-S@Pd@UiO and UiO-S@Pd@UiO), where the dual sites are in close proximity with strong electron interaction, is much lower than that of separate dual-site model, UiO-S@UiO_{25}@Pd@UiO (Fig. 4*C* and *SI Appendix*, Fig. S21). The results delineate that the high electron state of $Pd^{\delta+}$ caused by the intimate contact between the dual sites in UiO-S@Pd@UiO and UiO@Pd@UiO-S is prone to H_2 heterolysis on the Pd surface, which is almost consistent with the experimental results above (*SI Appendix*, Fig. S12).

To further gain insight into reaction paths, control experiments are also carried out in the presence of UiO@Pd@UiO-S and deuterated UiO@Pd@UiO-S, in latter of which the H^+ in -SO_3H is replaced by D^+ via acidifying treatment in DCl solution. The alcohol products [*m/z* (122): *m/z* (123) = 354: 32], consisting of the 1-phenylethanol (122) and 1-phenylethanol (D) (123) signals, over UiO@Pd@UiO-S can be identified by gas chromatography-mass spectrometry (GC-MS) after 3 min of reaction. For UiO@Pd@UiO-S with deuterated –SO_3D groups, the fragment peak area of 1-phenylethanol (D) has an apparent increase, leading to a discrepant ratio [*m/z* (122): *m/z* (123) = 354: 76], which explicitly unveils that D^+ ions participate in the reaction and account for an increased amount of C_8H_9OD (*SI Appendix*, Fig. S22). In addition, the transformation rates of acetophenone and its *para*-substituted derivatives (X = –OCH_3, –F, and –CH_3) are examined over UiO@Pd@UiO-S to obtain the Hammett plot (*SI Appendix*, Fig. S23). The $\log(k_x/k_h)$ values are linearly related to the Brown–Okamoto constant parameters (σ^+) with a negative slope, indicating that the hydrogenation process of acetophenone generates positively charged intermediates, possibly $PhCH_3CHO^{+6}$. Similar mechanism is also demonstrated in the dehydration process of 1-phenylethanol (*SI Appendix*, Fig. S24). By contrast, the linear relationship between $\log(k_x/k_h)$ and (σ^+) cannot be observed with UiO-S@UiO_{25}@Pd@UiO as a catalyst (*SI Appendix*, Fig. S25), suggesting that no cation intermediate is participated during the reaction. These results demonstrate that protons in UiO@Pd@UiO-S participate in the reaction intermediate formation; by contrast, protons are not involved in the intermediate generation over UiO-S@UiO_x@Pd@UiO (x = 0, 5.5, 14, and 25) but promote the dehydration step only (36).

To illustrate the possible proton source and how the proton concentration affects the catalytic reaction, a comprehensive proton-transfer model of UiO-S@UiO_x (x = 0 ~ 50 nm), in which $\boldsymbol{r}_0$ is the radius of the UiO-66-SO_3H core and ($\boldsymbol{r}$ - $\boldsymbol{r}_0$) is the radius of the UiO-66 interlayer, is constructed (*SI Appendix*, Figs. S26–S28) (42). Simulations using a commercial solver (COMSOL 6.0) indicate that the proton concentration at the interface between UiO-66-SO_3H and UiO-66 shell is very high when the UiO-66 spacing interlayer is absent ($\boldsymbol{r}$ - $\boldsymbol{r}_0$ = 0). Therefore, for both UiO-S@Pd@UiO and UiO@Pd@UiO-S catalysts, the proton concentration around Pd, resulting from UiO-66-SO_3H dissociation, remains high. This elevated proton concentration facilitates an efficient conversion to ethylbenzene,

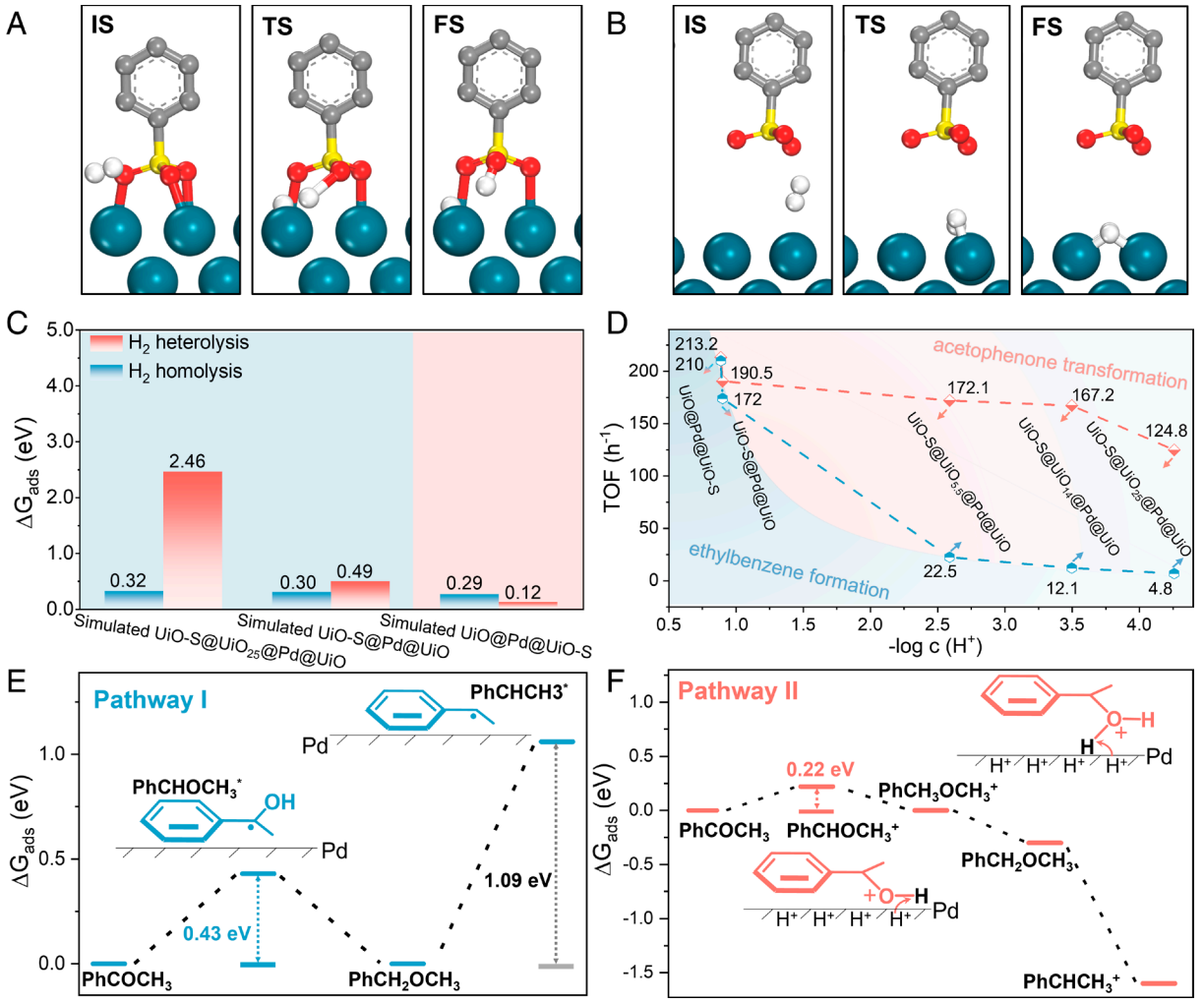

Fig. 4. DFT calculations and observed activity related to proton concentration around Pd NPs. (*A*–*C*) The geometry of initial state (IS), transition state (TS), and final state (FS) for the preferential H_2 heterolysis on simulated (*A*) UiO@Pd@UiO-S and the favorable H_2 homolysis on simulated (*B*) UiO-S@UiO_{25}@Pd@UiO from DFT, and (*C*) free energy barrier calculation of hydrogen heterolysis or homolysis on simulated UiO@Pd@UiO-S, UiO-S@Pd@UiO and UiO-S@UiO_{25}@Pd@UiO, respectively. (*D*) H^+ concentration [−log c(H^+)] dependent TOF of acetophenone transformation (above red dash line) and ethylbenzene formation (below blue dash line) over UiO-S@UiO_x@Pd@UiO (x = 0, 5.5, 14, and 25) and UiO@Pd@UiO-S. (*E* and *F*) Gibbs free energy diagram for the potential acetophenone transformation pathways over (*E*) separate dual-site model (simulating UiO-S@UiO_{25}@Pd@UiO, pathway I) and (*F*) intimate dual-site model (simulating UiO@Pd@UiO-S, pathway II).

consistent with reports that stronger acidity leads to higher reaction rates in the hydrodeoxygenation process (6). In fact, for UiO@Pd@UiO-S, the protons are able to directly bond with the C-O groups (*SI Appendix*, Fig. S22), following a proton-involved dehydration mechanism. Moreover, the concentrated protons probably contribute to the H_2 heterolysis turn-over limiting step, leading to the large isotope effect (*SI Appendix*, Fig. S12*A*) (39, 40), which further promotes the formation of ethylbenzene product with an optimal turnover frequency (TOF) of ~213.2 h^{-1} for acetophenone transformation (Fig. 4*D*). As the (r - r_0) value, i.e., UiO-66 interlayer thickness, increases, the proton concentration diminishes by several orders of magnitude. For UiO-S@UiO_x@Pd@UiO (x = 5.5, 14) with UiO-66 interlayer thickness of 5.5 nm and 14 nm, the proton amount around Pd remains at a relatively low level, which is unfavorable to the dehydration transformation of 1-phenylethanol (Fig. 4*D*) (6, 43), resulting in the reduced selectivity to ethylbenzene with inferior TOF (172.1 and 167.2 h^{-1}). For UiO-S@UiO_{25}@Pd@UiO with (r - r_0) of 25 nm, a tiny number of protons around Pd NPs lead to the limited reaction activity (TOF: 124.8 h^{-1}) and largely suppressed dehydration of 1-phenylethanol (Fig. 4*D* and *SI Appendix*, Table S5). Furthermore, the TOF for ethylbenzene formation is also calculated, which markedly reduces from 210 (for UiO@Pd@UiO-S) to 4.8 h^{-1} (for UiO-S@UiO_{25}@Pd@UiO) in parallel with the decreased trend of TOF for acetophenone conversion. The TOF values of controlled catalysts (x = 7.2, 84.5) also align closely with this trend (Fig. 4*D* and *SI Appendix*, Fig. S29). Notably, a higher TOF for UiO@Pd@UiO-S is obtained (210 h^{-1}) than that of UiO-S@Pd@UiO (172 h^{-1}), both of which possess comparable proton concentrations around Pd NPs. The results suggest that, in addition to the H^+ concentration, the strong electronic interaction of dual sites in UiO@Pd@UiO-S probably contributes to the ethylbenzene selectivity as well.

To further disclose the critical roles of proton concentration around Pd NPs in the reaction, DFT calculations have been conducted for the separate dual-site model (simulating UiO-S@UiO_{25}@Pd@UiO) and the intimate dual-site model (simulating UiO@Pd@UiO-S) as representatives (Fig. 4 *E* and *F*). A traditional hydrogenation process (pathway I) is verified over the separate case (Fig. 4*E*). At the beginning, acetophenone and H_2 are activated on Pd NPs, in which H_2 gas undergoes homolytic cleavage, generating Pd-H species on the Pd surface. Next, the C = O bond of acetophenone is coupled with the H active species to produce a $PhCHOCH_3^*$ intermediate with a reaction energy of 0.43 eV, which is included in the rate-determining step (RDS).

After that, 1-phenylethanol is further produced by combining $PhCHOCH_3^*$ with H species. Notably, a high reaction energy of 1-phenylethanol dehydration (1.09 eV) is observed (Fig. 4*E*), which indicates that the dehydration process is severely impeded due to the extremely low proton concentration around Pd NPs. Although similar hydrogenation process exists in UiO-S@UiO_x@Pd@UiO (x = 0, 5.5, and 14), increased proton concentrations around Pd NPs are favorable to promote the dehydration of 1-phenylethanol, leading to improved selectivity to ethylbenzene (43).

In comparison, over the intimate dual-site model (pathway II), both acetophenone and H_2 molecules are absorbed on the Pd surface at first, and H_2 is cleaved with a heterolysis process at the Pd-O interface due to the strong electron effect between Pd and $-SO_3H$ groups (Figs. 2 *F–H* and 4*A*). Simultaneously, according to the GC-MS results, the dissociative H^+ species generated from the adjacent UiO-66-SO_3H shell attacks the C = O bond directly, affording the carbocation intermediate ($PhCHOCH_3^+$) (*SI Appendix*, Figs. S22 and S23). This partial hydrogenation of the C = O bond is involved in the RDS with a small reaction energy of 0.22 eV according to the DFT results (Fig. 4*F*). Remarkably, this energy is much lower than that (0.43 eV) in pathway I, supporting the enhanced activity of UiO@Pd@UiO-S (Fig. 4*D*). Then, the generated $PhCHOCH_3^+$ intermediate combines with the H^- species from H_2 heterolysis, producing 1-phenylethanol, and the remaining H^+ from H_2 heterolysis overflows into the proton reservoir of the UiO-66-SO_3H shell. Subsequently, the C-O bonds of 1-phenylethanol capture the H^+ from the adjacent UiO-66-SO_3H shell, inducing a spontaneous dehydration process, which produces a carbocation intermediate ($PhCH_3CH^+$) (Fig. 4*F*). After that, $PhCH_3CH^+$ reacts with the H^- species, affording ethylbenzene product with high activity. Overall, the above results well prove that the spatial arrangement of Pd and Brønsted acid sites significantly affects the reaction pathways, in which the selectivity can be manipulated by rational control of the proximity degree between the dual sites.

The stability and reusability of UiO-S@UiO_{25}@Pd@UiO and UiO@Pd@UiO-S in the acetophenone transformation have been examined. To our delight, both catalytic activity and selectivity remain very well in the three consecutive runs (*SI Appendix*, Fig. S30). In addition, the structure and morphology of both catalysts are well preserved after recycling experiments (*SI Appendix*, Figs. S31 and S32). Encouraged by the outstanding selectivity and stability of UiO-S@UiO_{25}@Pd@UiO and UiO@Pd@UiO-S, the transformations of diverse aromatic ketones and aldehydes have been examined to evaluate the substrate tolerance (*SI Appendix*, Table S7). The results show that both catalysts can efficiently convert C = O bonds to the corresponding hydrogenation or dehydration products with similar high selectivity as that in the acetophenone transformation, which demonstrates the general applicability in the selective hydrodeoxygenation of diverse aromatic ketones and aldehydes by regulating the distance of the Pd and acid sites.

Discussion

In summary, we have developed a rational synthetic strategy of achieving the control of spatial distance of dual (metal and acid) sites based on MOF platform for switching the selectivity of acetophenone hydrodeoxygenation. By precisely regulating the thickness of the UiO-66 interlayer from 0 nm to 25 nm in multishell structured composites, UiO-S@UiO_x@Pd@UiO, the distance between Pd and acid sites can be accordingly controlled. Moreover, the relative location of both sites was further adjusted in UiO@Pd@UiO-S by coating UiO-66-SO_3H shell outside Pd NPs. The homolytic cleavage of H_2 molecules occurred over UiO-S@UiO_{25}@Pd@UiO due to the weak electron effect on Pd NPs, with which a routine hydrogenation reaction pathway was demonstrated in the acetophenone transformation, leading to high selectivity to 1-phenylethanol (>94%). By reducing the distance between Pd and acid sites in UiO-S@UiO_x@Pd@UiO (x = 5.5, 14), increased proton concentration around Pd NPs promoted the dehydration reactivity of 1-phenylethanol to afford both 1-phenylethanol and ethylbenzene products. When x = 0, the UiO-S@Pd@UiO with the dual sites in close proximity gave high selectivity to ethylbenzene (>99%). Significantly, for UiO@Pd@UiO-S with inverse core/shell, strong electronic interaction between dual sites gave rise to the heterolysis of H_2 molecules. As a result, the high proton concentration around Pd sites and strong electronic interaction of Pd surface over UiO@Pd@UiO-S, led to excellent activity (TOF up to 213.2 h^{-1}) and complete selectivity to ethylbenzene via a proton-involved pathway. This work provides a synthetic protocol in the precise control of the proximity and spatial distribution between the dual sites at the nanoscale and unveils their critical roles in regulating reaction pathway and dominating catalytic performance.

Materials and Methods

Synthesis of UiO-66. The preparation of UiO-66 was carried out according to previous work with minor modifications (44). Typically, 40.8 mg of $ZrCl_4$, 26.6 mg of H_2BDC and 0.5 mL of acetic acid (CH_3COOH) were ultrasonically dispersed in 10 mL of N,N-dimethylformamide (DMF). After that, the mixed solution was sealed into a 20 mL vessel and allowed to react at 120 °C for 24 h. The as-synthesized UiO-66 was filtered and washed with acetone and activated at 60 °C for 12 h under vacuum.

Synthesis of UiO-66-SO_3H. The synthesis was based on a previous report with modifications (44). Typically, 48 mg of $ZrCl_4$, 27.4 mg of H_2BDC, 11.04 mg of H_2BDC-SO_3Na, 2.36 mL of CH_3COOH and 10 μL of H_2O were dispersed in 10 mL DMF solvent. Then, the mixture was added to a 20 mL vial and ultrasonicated for 10 min. After that, the well-dispersed mixture in a tightly capped flask was placed at 120 °C for 24 h. The produced white suspensions were collected by centrifugation, washed three times with DMF and sequentially immersed in acetone for 24 h. Finally, the white powder was dried at 60 °C under vacuum for 12 h.

Synthesis of Pd NPs. The Pd NPs were synthesized with a reported precipitation method (31). Typically, an aqueous solution (8 mL) containing 105 mg of polyvinyl pyrrolidone (PVP), 60 mg of L-ascorbic acid, and 5 mg of KBr was added to a 20 mL vial. The solution was preheated under magnetic stirring at 80 °C for 10 min. Next, 3 mL of another aqueous solution containing 63.2 mg of K_2PdCl_4 was added using a pipette. Then, the reaction proceeded at 80 °C for 3 h. After that, the products were collected by centrifugation and washed 3 times with a water/acetone mixture to remove excess PVP, L-ascorbic acid, and KBr. Finally, the product was redispersed in 5 mL of DMF solvent.

Synthesis of UiO-S@UiO_x@Pd@UiO (x = 0, 5.5, 14, and 25). When x = 0, the UiO-S@ Pd@UiO in the absence of UiO-66 interlayer, featuring a sandwiched nanostructure, was prepared with the following steps according to a previous report with minor modifications (32). Typically, 10 mg of UiO-66-SO_3H, 100 mg of PVP, 700 μL of CH_3COOH, 50 μL of Pd NPs (0.04 mol/L DMF solution) and 16.7 mg of $ZrCl_4$ were mixed in 10 mL DMF in a 20 mL vial followed by ultrasonic treatment for 15 min. To guarantee the amount of attached Pd NPs on the MOF surface, extra Pd NPs were added into the above mixture during the growth outermost shell. In detail, 30 μL of Pd NPs (0.04 mol/L DMF solution) and 12.5 mg of BDC were dissolved into the mixture with ultrasonic treatment for another 25 min. Finally, the mixture in the capped vessel was reacted at 120 °C for 2 h.

For the synthesis of UiO-S@$UiO_{5.5}$ and UiO-S@UiO_{25}, 10 mg of UiO-66-SO_3H, 100 mg of PVP, 700 μL of CH_3COOH, 16.7 mg of $ZrCl_4$ and 10 mL of DMF were first mixed in a 20 mL glass vessel with ultrasonic treatment for 15 min. Then, 12.5 mg of H_2BDC was added into the tightly capped vessel with ultrasonic treatment and reacted at 120 °C for 1 h or 2 h, respectively. The synthetic methods of UiO-S@

$UiO_{84.5}$ followed a procedure identical to UiO-S@$UiO_{25,}$ except for adjusting the amount of $ZrCl_4$ and BDC to 33.4 mg and 25 mg, respectively. For the synthesis of UiO-S@$UiO_{7.2}$ or UiO-S@UiO_{14}, the mixture of 25 mg or 20 mg of UiO-66-SO_3H, 16.7 mg of $ZrCl_4$, 100 mg of PVP and 700 μL of CH_3COOH was dissolved in 10 mL DMF with ultrasonic treatment for 15 min. After that, 12.5 mg of H_2BDC was added with ultrasonic treatment for another 25 min, and then the mixture in the tightly capped glass vessel was reacted at 120 °C for 1 h. All the UiO-S@UiO_x (x = 5.5, 7.2, 14, 25, and 84.5) products were collected by centrifugation followed by washing with DMF/acetone three times and drying in vacuum at 60 °C for 6 h.

The UiO-S@UiO_x@Pd@UiO (x = 5.5, 14, 25) composites were prepared as follows. Typically, 10 mg of the above synthesized UiO-S@UiO_x (x = 5.5, 14, and 25), 100 mg of PVP, 700 μL of CH_3COOH, 50 μL of Pd NPs (0.04 mol/L DMF solution) and 16.7 mg of $ZrCl_4$ were mixed with 10 mL of DMF in a 20 mL glass vial followed by ultrasonic treatment for 15 min. Then, to guarantee the amount of attached Pd NPs on the MOF surface, extra Pd NPs were added into the above mixture during the growth of the outermost shell. In detail, 30 μL of Pd NPs (0.04 mol/L DMF solution) and 12.5 mg of H_2BDC were dissolved into the mixture with ultrasonic treatment for another 25 min. After that, the capped vial was reacted at 120 °C for 2 h. The products were collected via centrifugation and washed with acetone/DMF for three times. The as-synthesized UiO-S@UiO_x@Pd@UiO (x = 5.5, 14, and 25) composites were dried at 60 °C under vacuum.

Synthesis of UiO@Pd@UiO-S. The UiO@Pd@UiO-S with a sandwiched nanostructure was synthesized by the hydrothermal method according to a previous report with minor modifications (32). Typically, 10 mg of UiO-66, 100 mg of PVP, 700 μL of CH_3COOH, 50 μL of Pd NPs and 16.7 mg of $ZrCl_4$ were first mixed with 10 mL DMF in a 20 mL vial, followed by ultrasonic treatment for 15 min. After that, 30 μL of Pd NPs (0.04 mol/L DMF solution) and 20.1 mg of H_2BDC-SO_3Na were dissolved into the mixture with ultrasonic treatment for another 25 min. Then, the mixture was reacted at 120 °C for 2 h. All products were collected by centrifugation and washed three times with DMF and acetone to remove the residual precursor. Finally, the product was dried under vacuum for 6 h to afford UiO@Pd@UiO-S.

Synthesis of UiO@Pd@UiO-S(D). The synthetic steps of UiO@Pd@UiO-S(D) were as follows: 20 mg of UiO@Pd@UiO-S was dispersed in 1 mL of DCl/D_2O (0.2 wt%) solvent and stirred for 40 min. The product was collected via centrifugation and washed with DMF and acetone for three times. Then, it was dried under vacuum at 60 °C for 6 h.

Catalytic Transformation of Acetophenone Over Different Catalysts. Prior to the reaction, all catalysts were acidized in 0.1 M HCl for 1 h and washed with H_2O/acetone for three times. Then, a mixture of 15 mg UiO-S@UiO_x@Pd@UiO (x = 0, 5.5, 14, and 25) or 15 mg UiO@Pd@UiO-S or 15 mg UiO@Pd@UiO-S(D), 0.2 mmol of acetophenone and 3 mL of ethanol were added into a 25 mL flask with a H_2 balloon. After that, the reaction proceeded for 3 h [or 3 min for UiO@Pd@UiO-S(D) catalyst] at 60 °C with a H_2 balloon. After completion of the reaction, 200 μL of the resultant mixture was added to 1 mL of ethyl acetate. Upon adequate shaking, the mixture was centrifuged. Then, 600 μL of sample in the upper solution was detected by GC or GC-MS.

Time-Dependent Catalytic Acetophenone Transformation. Typically, a mixture of 15 mg UiO-S@UiO_x@Pd@UiO (x = 0, 5.5, 14, and 25) or UiO@Pd@UiO-S, 0.2 mmol of acetophenone and 3 mL of ethanol were added into a 25 mL flask with a H_2 balloon. Then, the reaction was initiated at 60 °C. To obtain the kinetic profiles, 80 μL of the reaction mixture was sampled every 10 min during the reaction process. Then, the reaction mixture was added to 1 mL of ethanol before centrifugation. The products dissolved in the liquid supernatant were detected by GC.

Catalytic Transformation of Diverse Aromatic Ketones and Aldehydes Over UiO-S@UiO_{25}@Pd@UiO and UiO@Pd@UiO-S. After acid treatment of all catalysts, a mixture of 15 mg UiO-S@UiO_{25}@Pd@UiO or UiO@Pd@UiO-S (or 20 mg UiO-S@UiO_{25}@Pd@UiO or UiO@Pd@UiO-S for vanillin), 0.2 mmol of *p*-methylacetophenone, *p*-methoxyacetophenone, *p*-fluoroacetophenone, and furfural (or 0.1 mmol of vanillin), 4 mL of ethanol (or 3 mL of 1-butanol for vanillin and furfural) were added into a 25 mL flask with a H_2 balloon. The reaction was then carried out for 3 h at 60 °C (or 5 h at 90 °C for vanillin, 2 h at 75 °C for furfural). After reaction, 200 μL of the resulting mixture was added to 1 mL of ethyl acetate. Upon adequate shaking, the mixture was centrifuged. Then, 600 μL of the sample in the upper solution was detected by GC.

H_2 Gas TPD. The H_2 TPD experiments were performed on a Micromeritics AutoChem II chemisorption analyzer that was connected to a Pfeiffer OmniStar mass spectrometer. In a typical experiment, a 50 mg sample was oxidized in O_2 gas at 100 °C for 0.5 h, reduced in 10% H_2/He at 120 °C for 0.5 h and then purged with He at 120 °C for 1 h. Next, the sample was cooled down to room temperature in He gas; then, H_2 gas was introduced into the sample until saturation. Subsequently, the sample was purged with He at 25 °C for 1 h, and then the sample temperature was gradually increased at a heating rate of 10 °C min^{-1} in He gas from 25 to 200 °C while recording the TPD data.

DRIFTS Experiments. All DRIFTS experiments were carried out with the samples on a Nicolet iS10 spectrometer equipped with a mercury cadmium telluride (MCT) detector and a low-temperature reaction chamber (Praying Mantis Harrick). Prior to the measurement, the sample was sufficiently activated at 393 K for 24 h to eliminate solvent or other adsorbates and enable the adsorption sites to be exposed. Upon the activation treatment, a certain amount of the powdery sample was placed into the reflectance cell and purged by flowing Ar gas (25 mL/min) to obtain a stable background spectrum. Then, the stream of CO/Ar (10%) mixture gas or acetophenone loaded in Ar gas was carried into the sample cell at a rate of 25 mL/min until saturation. The spectra were collected for 256 scans at 4 cm^{-1} resolution during Ar gas purging or elevating temperature.

Deuterium Labeling Experiments. To calculate the KIE [K_L/K_H, the rate constant for light substrate (K_L) and heavy substrate (K_H)], deuterium-labeling experiments over different catalysts were carried out under the same conditions as the above catalytic procedure, except that the hydrogen source of H_2 gas was replaced by D_2 gas. Moreover, the conversion is controlled at a low level of 10 to 20%. All the products were identified by GC or GC-MS equipment.

Recycling Experiments. For the catalytic recycling experiments, the catalysts UiO-S@UiO_{25}@Pd@UiO and UiO@Pd@UiO-S were separated by centrifugation after the reaction and thoroughly washed twice with 5 mL acetone. Then, the catalyst was ready for the next run.

Proton Concentration Transfer Model for the MOF Composites. A Nernst–Planck–Poisson (NPP) model was used to predict the steady-state distribution of the proton concentration within the MOF composites. The series of UiO-66-based MOFs show a regular octahedral morphology. To simplify the calculations, a spherically symmetric geometry with a UiO-66-SO_3H core and a UiO-66 shell is constructed. The core radius ($\boldsymbol{r_0}$) is set to 100 nm, approximately matching the characterization results observed in the TEM images. The overall system radius is chosen to be sufficiently large ($\boldsymbol{r_{tot}}$ = 500 nm) to ensure that the transport of H^+ at the interface between UiO-66-SO_3H and UiO-66 is not affected.

Protons originate from the dissociation of the sulfonic acid group (−SO_3H) and ethanol; therefore, we have the −SO_3H dissociation equilibrium in the region of UiO-66-SO_3H (Eq. **1**) and the C_2H_5OH dissociation equilibrium in the entire region (Eq. **2**) as equality constraints for steady-state calculation.

$$C_{H^+}C_{-SO_3^-} = kC_{-SO_3H}C^{\theta} \quad (0 < r \le r_0), \qquad [1]$$

$$C_{H^+}C_{C_2H_5O^-} = k_sC^{\theta 2} \quad (r > 0), \qquad [2]$$

$$C_{-SO_3H} + C_{-SO_3^-} = C_0 \quad (0 < r \le r_0), \qquad [3]$$

where $\boldsymbol{C_{H^+}}$, $\boldsymbol{C_{-SO_3^-}}$, and $\boldsymbol{C_{-SO_3H}}$ represent the concentration of the corresponding species; $\boldsymbol{k}$, whose values are discussed in (*SI Appendix*, Fig. S28) stands for the acidic dissociation constant of −SO_3H; $\boldsymbol{k_s}$ is the ionic product of ethanol (the dissociation of C_2H_5OH is so weak that it has little effect on the proton concentration contribution; thus, it is simply set as 10^{-19}, which is the ionic product constant of liquid ethanol at room temperature); $\boldsymbol{r_0}$ is the radius of the UiO-66-SO_3H core; and $\boldsymbol{C^{\theta}}$ is 1 M, which is used for nondimensionalization. $\boldsymbol{C_0}$ is 1.03 M, representing the total concentration of −SO_3H and −SO_3^-, and it can be determined based on the lattice structure of UiO-66-SO_3H as follows:

$$C_0 = \frac{\text{the number of organic ligands per unit cell}/4}{\text{cell parameters}^2}. \quad [4]$$

Due to the hindrance caused by the MOF skeleton, we assumed that convection does not contribute to mass transfer within the MOF composites. Therefore, the steady-state Nernst–Planck equations can be expressed as follows:

$$D_i^{UiO-S}\nabla^2\left[H^+\right] + \nabla\frac{D_i^{UiO-S}C_i z_i F}{RT}\nabla\phi = 0 (0 < r \le r_0), \quad [5]$$

$$D_i^{UiO}\nabla^2\left[H^+\right] + \nabla\frac{D_i^{UiO}C_i z_i F}{RT}\nabla\phi = 0 (r \ge r_0), \quad [6]$$

where $\boldsymbol{C_i}$ and $\boldsymbol{z_i}$ represent the concentration and ionic charge of solution species (i = H^+ and C_2H_5OH), respectively; $\boldsymbol{D_i^{UiO-S}}$ and $\boldsymbol{D_i^{UiO}}$ account for the diffusion coefficient within UiO-66-SO_3H and UiO-66 of species $\boldsymbol{i}$, respectively; $\boldsymbol{F}$ is the Faraday constant; $\boldsymbol{R}$ is the molar gas constant; $\boldsymbol{T}$ accounts for the temperature of this system (333.15 K); and Φ stands for the potential.

The potential Φ in Eqs. **5** and **6** is determined by the Poisson equation:

$$\nabla^2\phi = -\frac{F(-C_{-SO_3^-} + \sum_i Z_i C_i)}{\varepsilon_0\varepsilon_r}, \quad [7]$$

where $\boldsymbol{\varepsilon_0}$ accounts for the vacuum permittivity, and $\boldsymbol{\varepsilon r}$is the relative permittivity of this system. The relative permittivity is discussed in (*SI Appendix*, Fig. S28) and is assumed to be constant throughout the entire framework.

A zero flux boundary condition is applied to the left boundary ($\boldsymbol{r} = 0$) of the NNP equation. The right boundary ($\boldsymbol{r} = \boldsymbol{r_{tot}}$) corresponds to the species concentration and potential of the bulk solution, which is built using the Dirichlet boundary condition given by

$$c_{i,r=r_{tot}} = c_{i,bulk}, \quad [8]$$

$$\phi_{r=r_{tot}} = 0. \quad [9]$$

The model was transformed into one-dimensional by leveraging the spherical symmetry of the system. Subsequently, the geometric construction and steady-state NPP simulation were conducted using COMSOL Multiphysics version 6.0. The General Form PDE module within COMSOL was utilized to formulate the Nernst–Planck equation and Poisson equation in spherically symmetric coordinates. To accurately resolve the large concentration gradients, the mesh size at the boundaries of region 1 and region 2 was set to be less than 0.01 nm, with a maximum cell growth rate set at 1.1. The coupled equations were solved by employing a MUMPS solver with a nonlinear automatic Newton method. The relative tolerance was set to 0.001.

DFT Calculation Method. Spin-polarized DFT calculations were performed via the Vienna ab initio simulation package (VASP 5.4.4) (45). The exchange-correlation energetics were described by the Perdew–Burke–Ernzerhof functional within the generalized gradient approximation method (46, 47). Taking the effect of weak interactions into consideration, van der Waals interactions were treated using the correction within Grimme's scheme (DFT-D3) (48). In detail, the three-layer slab model was constructed based on the Pd (100) surface, and a 20 Å vacuum layer thickness was placed to avoid the effect of mirror interaction. In geometric optimization, a 2 × 2 × 1 Γ-centered k-point mesh grid and 450 eV cut-off energy were adopted, and the convergence standards of energy and force were selected as 10^{-5} eV and 0.02 eV/Å, respectively. To obtain more accurate system energy information, a 4 × 4 × 1 Γ-centered k-point mesh grid was adopted for the subsequent self-consistent field calculation. The climbing-image nudged elastic band (CI-NEB) method was performed to obtain thermodynamic energy barriers (49), with the energy and force convergence standards set to 10^{-5} eV and 0.03 eV/Å, respectively. According to the calculation models, the variation in the Gibbs free energy of each step (ΔG) can be calculated from the following equation (50):

$$\Delta G = \Delta E + \Delta ZPE - T\Delta S, \quad [10]$$

where ΔE is the difference in electronic energy in the ground state obtained from self-consistent calculation; ΔZPE is the difference in zero point energy; T is the Kelvin temperature (T = 298.15 K); and ΔS is the difference in entropy.

Data, Materials, and Software Availability. All study data are included in the article and/or *SI Appendix*.

ACKNOWLEDGMENTS. This work is supported by the National Key Research and Development Program of China (2021YFA1500402), the Strategic Priority Research Program of the Chinese Academy of Sciences (XDB0450302), the National Natural Science Foundation of China (22331009, U22A20401, 22201182), the Postdoctoral Fellowship Program of China Postdoctoral Science Foundation (GZC20232532), and the Key Project of Natural Science Foundation of Anhui Province (2508085ZD002). The calculations in this work are supported by the Supercomputing Center of University of Science and Technology of China and Hefei Advanced Computing Center for providing computational resources.

Author affiliations: [a]Hefei National Research Center for Physical Sciences at the Microscale, College of Chemistry and Materials Science, University of Science and Technology of China, Hefei, Anhui 230026, People's Republic of China; [b]Department of Power Engineering, School of Energy, Power and Mechanical Engineering, North China Electric Power University, Baoding, Hebei 071003, People's Republic of China; [c]School of Information and Electronic Engineering, Shandong Technology and Business University, Yantai 264005, People's Republic of China; and [d]School of Materials Science and Engineering and Beijing Innovation Center for Engineering Science and Advanced Technology, College of Engineering, Peking University, Beijing 100871, People's Republic of China

1. R. Qu, K. Junge, M. Beller, Hydrogenation of carboxylic acids, esters, and related compounds over heterogeneous catalysts: A step toward sustainable and carbon-neutral processes. *Chem. Rev.* **123**, 1103–1165 (2023).
2. P. Del Campo, C. Martinez, A. Corma, Activation and conversion of alkanes in the confined space of zeolite-type materials. *Chem. Soc. Rev.* **50**, 8511–8595 (2021).
3. X. Pan, F. Jiao, D. Miao, X. Bao, Oxide-zeolite-based composite catalyst concept that enables syngas chemistry beyond Fischer-tropsch synthesis. *Chem. Rev.* **121**, 6588–6609 (2021).
4. J. Fu *et al.*, C-O bond activation using ultralow loading of noble metal catalysts on moderately reducible oxides. *Nat. Catal.* **3**, 446–453 (2020).
5. H. Ning *et al.*, Selective upgrading of biomass-derived benzylic ketones by (formic acid)–Pd/HPC–NH_2 system with high efficiency under ambient conditions. *Chem* **7**, 3069–3084 (2021).
6. W. Liu *et al.*, Ambient-pressure and low-temperature upgrading of lignin bio-oil to hydrocarbons using a hydrogen buffer catalytic system. *Nat. Energy* **5**, 759–767 (2020).
7. J. Zhang *et al.*, Control of interfacial acid–metal catalysis with organic monolayers. *Nat. Catal.* **1**, 148–155 (2018).
8. Q. Zhang, S. Gao, J. Yu, Metal sites in zeolites: Synthesis, dion, and catalysis. *Chem. Rev.* **123**, 6039–6106 (2023).
9. Q. Zhu *et al.*, Enhanced CO_2 utilization in dry reforming of methane achieved through nickel-mediated hydrogen spillover in zeolite crystals. *Nat. Catal.* **5**, 1030–1037 (2022).
10. J. Zečević, G. Vanbutsele, K. P. de Jong, J. A. Martens, Nanoscale intimacy in bifunctional catalysts for selective conversion of hydrocarbons. *Nature* **528**, 245–254 (2015).
11. K. Cheng *et al.*, Maximizing noble metal utilization in solid catalysts by control of nanoparticle location. *Science* **377**, 204–208 (2022).
12. J. He *et al.*, Zeolite-tailored active site proximity for the efficient production of pentanoic biofuels. *Angew. Chem. Int. Ed. Engl.* **60**, 23713–23721 (2021).
13. P. B. Weisz, E. W. Swegler, Stepwise reaction on separate catalytic centers: Isomerization of saturated hydrocarbons. *Science* **126**, 31–32 (1957).
14. J. Francis *et al.*, Design of improved hydrocracking catalysts by increasing the proximity between acid and metallic sites. *Appl. Catal. A.* **409–410**, 140–147 (2011).
15. S. Tian *et al.*, High-efficiency hydrocracking of polyolefin plastics by controlling intimacy between Pt clusters and zeolite acid sites. *J. Am. Chem. Soc.* **147**, 30268–30276 (2025).
16. J. Zhu *et al.*, Ultrafast encapsulation of metal nanoclusters into MFI zeolite in the course of its crystallization: Catalytic application for propane dehydrogenation. *Angew. Chem. Int. Ed. Engl.* **59**, 19669–19674 (2020).
17. L. Liu *et al.*, Regioselective generation and reactivity control of subnanometric platinum clusters in zeolites for high-temperature catalysis. *Nat. Mater.* **18**, 866–873 (2019).
18. H. Furukawa, K. E. Cordova, M. O'Keeffe, O. M. Yaghi, The chemistry and applications of metal-organic frameworks. *Science* **341**, 1230444 (2013).
19. H. C. Zhou, S. Kitagawa, Metal–organic frameworks (MOFs). *Chem. Soc. Rev.* **43**, 5415–5418 (2014).
20. Y. Zhang *et al.*, Metal-organic framework with space-partition pores by fluorinated anions for benchmark C_2H_2/CO_2 separation. *J. Am. Chem. Soc.* **146**, 17220–17229 (2024).
21. J. Liu *et al.*, MOF-enabled confinement and related effects for chemical catalyst presentation and utilization. *Chem. Soc. Rev.* **51**, 1045–1097 (2022).
22. X. Zhao, Y. Wang, D.-S. Li, X. Bu, P. Feng, Metal–organic frameworks for separation. *Adv. Mater.* **30**, 1705189 (2018).
23. P. M. Stanley, J. Haimerl, N. B. Shustova, R. A. Fischer, J. Warnan, Merging molecular catalysts and metal-organic frameworks for photocatalytic fuel production. *Nat. Chem.* **14**, 1342–1356 (2022).
24. A. Dhakshinamoorthy, Z. Li, S. Yang, H. Garcia, Metal-organic framework heterojunctions for photocatalysis. *Chem. Soc. Rev.* **53**, 3002–3035 (2024).
25. Q. Yang, Q. Xu, H.-L. Jiang, Metal-organic frameworks meet metal nanoparticles: Synergistic effect for enhanced catalysis. *Chem. Soc. Rev.* **46**, 4774–4808 (2017).
26. K. Sabyrov, J. Jiang, O. M. Yaghi, G. A. Somorjai, Hydroisomerization of n-hexane using acidified metal-organic framework and platinum nanoparticles. *J. Am. Chem. Soc.* **139**, 12382–12385 (2017).

27. E. S. Gutterod *et al.*, Hydrogenation of CO_2 to methanol by Pt nanoparticles encapsulated in UiO-67: Deciphering the role of the metal–organic framework. *J. Am. Chem. Soc.* **142**, 999–1009 (2020).
28. J. Chen, Y. Wang, F. Wang, Y. Li, Photo-induced switching of CO2 hydrogenation pathway towards CH3OH production over Pt@UiO-66-NH2(Co). *Angew. Chem. Int. Ed. Engl.* **62**, e2022181 (2023).
29. C. Fang *et al.*, Modifiers versus channels: Creating shape-selective catalysis of metal nanoparticles/porous nanomaterials. *Angew. Chem. Int. Ed. Engl.* **60**, 976–982 (2020).
30. J. H. Cavka *et al.*, A new zirconium inorganic building brick forming metal–organic frameworks with exceptional stability. *J. Am. Chem. Soc.* **130**, 13850–13851 (2008).
31. M. Jin *et al.*, Synthesis of Pd nanocrystals enclosed by 100 facets and with sizes < 10 nm for application in CO oxidation. *Nano Res.* **4**, 83–91 (2010).
32. M. Zhao *et al.*, Metal-organic frameworks as selectivity regulators for hydrogenation reactions. *Nature* **539**, 76–80 (2016).
33. M. Guo *et al.*, The promotion effect of π-π interactions in Pd NPs catalysed selective hydrogenation. *Nat. Commun.* **13**, 1770 (2022).
34. X. Yuan *et al.*, Selective deoxygenation of biomass-derived carbonyl compounds on Zn via electrochemical Clemmensen reduction. *Nat. Catal.* **7**, 43–54 (2024).
35. Z. H. Yin *et al.*, A green and efficient electrocatalytic route for the highly-selective oxidation of C-H bonds in aromatics over 1D Co3O4-based nanoarrays. *Angew. Chem. Int. Ed. Engl.* **63**, e202415044 (2024).
36. M. Chen, N. Maeda, A. Baiker, J. Huang, Hydrogenation of acetophenone on Pd/silica–alumina catalysts with tunable acidity: Mechanistic insight by in situ ATR-IR spectroscopy. *ACS Catal.* **8**, 6594–6600 (2018).
37. X. Shi *et al.*, Metal–support frontier orbital interactions in single-atom catalysis. *Nature* **640**, 668–675 (2025).
38. Q. Deng *et al.*, H^+-H^- pairs in partially oxidized MAX phases for bifunctional catalytic conversion of furfurals into linear ketones. *Angew. Chem. Int. Ed. Engl.* **62**, e202211461 (2023).
39. T. Bartholomeyzik *et al.*, Kinetics and mechanism of the palladium-catalyzed oxidative arylating carbocyclization of allenynes. *J. Am. Chem. Soc.* **140**, 298–309 (2018).
40. R. P. Bell, Recent advances in the study of kinetic hydrogen isotope effects. *Chem. Soc. Rev.* **3**, 513–544 (1974).
41. X. Lei *et al.*, High-entropy single-atom activated carbon catalysts for sustainable oxygen electrocatalysis. *Nat. Sustain.* **6**, 816–826 (2023).
42. D. Bohra, J. H. Chaudhry, T. Burdyny, E. A. Pidko, W. A. Smith, Modeling the electrical double layer to understand the reaction environment in a CO_2 electrocatalytic system. *Energy Environ. Sci.* **12**, 3380 (2019).
43. M. A. Mellmer *et al.*, Effects of chloride ions in acid-catalyzed biomass dehydration reactions in polar aprotic solvents. *Nat. Commun.* **10**, 1132 (2019).
44. A. Schaate *et al.*, Modulated synthesis of Zr-based metal—organic frameworks: From nano to single crystals. *Chem.-Eur. J.* **17**, 6643–6651 (2011).
45. J. Hafner, Simulations of materials using VASP: Density functional theory and beyond. *J. Comput. Chem.* **29**, 2044–2078 (2008).
46. I. C. Lin, A. P. Seitsonen, I. Tavernelli, U. Rothlisberger, Structure and dynamics of liquid water from ab initio molecular dynamics comparison of BLYP, PBE, and rev-PBE density functionals with and without van der waals corrections. *Comput. Theor. Chem.* **8**, 3902–3910 (2012).
47. S. Grimme, Semiempirical GGA type density functional constructed with a long range dispersion correction. *J. Comput. Chem.* **27**, 1787–1799 (2006).
48. J. Moellmann, S. Grimme, DFT-D3 study of some molecular crystals. *J. Phys. Chem. C* **118**, 7615–7621 (2014).
49. D. Sheppard, P. Xiao, W. Chemelewski, D. D. Johnson, G. Henkelman, A generalized solid-state nudged elastic band method. *J. Chem. Phys.* **136**, 074103 (2012).
50. A. A. Peterson, F. Abild-Pedersen, F. Studt, J. Rossmeisl, J. K. Nørskov, How copper catalyzes the electroreduction of carbon dioxide into hydrocarbon fuels. *Energy Environ. Sci.* **3**, 1311–1315 (2010).